

CaO NANOPARTICLES AS A POTENTIAL DRUG DELIVERY AGENT FOR BIOMEDICAL APPLICATIONS

A. R. BUTT^a, S. EJAZ^b, J. C. BARON^{b,d}, M. IKRAM^c, S. ALI^{a,c*}

^a*Material and Nano Science Research Lab (MNRL), Department of Physics, Government College University Lahore, 54000, Punjab, Pakistan.*

^b*Department of Clinical Neurosciences, Stroke Research Group, University of Cambridge, Cambridge, UK.*

^c*Solar Applications Research Lab, Department of Physics, Government College University Lahore, 54000, Punjab, Pakistan.*

^d*INSERM U894, Hôpital Sainte-Anne, Université Paris Descartes/Sorbonne Paris Cité, Paris, France*

This work demonstrates chemical co-precipitation route to synthesize calcium oxide (CaO) nanoparticles, which were used in various biomedical applications. The resulted nanoparticles were fully characterized and then conducted in rats for biomedical responses as bio-distribution, bio-labeling and cytotoxicity. The analysis of X-ray diffraction (XRD) data showed the particle size as ~11 nm. The thermal behavior was studied using Thermogravimetric Analysis and Differential Scanning Calorimetry (TGA/DSC) while compositional analysis was performed by Fourier Transform Infra-Red (FTIR) spectroscopy and Energy Dispersive X-rays (EDX) coupled with Scanning Electron microscope (SEM). The obtained results confirmed the phase purity and presence of CaO nanoparticles. Polyvinyl alcohol (PVA) was used as a protective shield over nanoparticles to functionalize them for biomedical assessments. Areas of necrosis, haemorrhages and degenerations were seen histopathologically in kidney, liver and brain after three months of administration of CaO nanoparticles in the order of severity. MRI could not detect any lesions after 15 minutes distal middle cerebral artery (MCA) occlusion. Immunofluorescence and Immunohistochemistry study also could not detect any neuro-inflammation.

(Received May 8, 2015, Accepted July 17, 2015)

Keywords: Calcium oxide; XRD; Toxicity; Antimicrobial, FTIR, Bio labeling

1. Introduction

In the past decade, researchers have been immensely focused on nanotechnology and profoundly efforts to investigate the electrical, optical and magnetic properties of nanomaterial's [1]. These peculiarities can be modulated for wide nano-biomedical applications [2-7]. A variety of nanoparticle based therapeutics have improved the efficacy and reduced the toxicity of drugs, subsequently, making them potential candidates to overcome the separation and purification of cells, biological barriers and targeted drug delivery agents [8-10].

These advances and drug discoveries still have a limited approach towards the treatments of neurological disorder and can overcome the hindrance using nano-diagnostics drugs targeting the central nervous-system (CNS). In this scenario, an efficient delivery of many potential theraganostics compounds to the particular zone of the brain is facing different barriers [11]. Therefore, the worldwide market of CNS nanodrugs is critically under development and their growth rate over 500% would have compared to cardiovascular drugs [12]. Fewer drugs, with

*Corresponding author: salamatali@gcu.edu.pk

higher lipid solubility and molecular mass < 400 – 500 Da, can penetrate across blood-brain barriers [13].

The transport mechanism through these impermeable barriers can be made possible by the effective functionalization of nanoparticles (NPs). This functionalization changes a number of characteristics as desired for smart drug delivery as transport capabilities, specific organ binding and the ultimate excretion of NPs. These modulations can possibly enhance the kinetics and efficiency of drugs through different tissues. When NPs have improved for drug-carrying and transport capabilities, the biomarkers like fluorescent dyes are used *in vivo* ocular imaging [14].

Recently, with the significance of healthcare, a large number of studies have been accomplished to make effective conjugation of biomolecules onto inorganic nanoparticles. These nanoparticles with long-term effects have not been clearly examined and are associated with inflammation, immunogenicity, toxicity, long-term tissue damage and carcinogenesis. Therefore, it is essential to establish such kind of inorganic nanoparticles that have the potential to minimize undesirable effects due to long-term exposure. These NPs can improve the short-term therapeutics by modulating their circulation, biodegradation and stability on *in vivo* studies [15]. Researchers are also conducting a lot of experiments on the antimicrobial action of nanoparticles but clinically not appreciable due to their lesion and toxic effects [16]. Inorganic antimicrobial agents are progressively used to control microorganism in various fields, particularly in dentistry. It has been demonstrated the characteristics of inorganic nanomaterials depend upon their morphologies, so the particle size of metal oxides is important in anti-microorganism activity [17]. The antimicrobial aspects of oxides have high microbial resistance and thermal stability as reported for various inorganic metal oxide MgO, ZnO and CaO [18]. Therefore, controlled synthesis techniques are primarily focused to attain nanoparticles with tailored morphological configurations and size distributions [19- 21].

But calcium oxide NPs has significant consideration due to its histocompatibility and antimicrobial potential [22, 23], tissue dissolution [24], and capability to inactivate microbial endotoxin [25, 26]. It exhibits cubic lattice showing anisotropic catalytic behavior and used as dopant to stabilize metal-oxide. Few research groups reported the synthesis of nano-CaO by using thermal decomposition and sol-gel techniques [18].

In the present work, CaO nanoparticles were prepared using chemical precipitation process. The resulted nanoparticles were used in biomedical assessments such as bio-distribution, bio-labeling and cytotoxicity after IV administration in rats.

2. Experimental details

2.1. Materials

Anhydrous calcium chloride (CaCl_2), sodium hydroxide (NaOH), polyvinyl alcohol (PVA) and ethanol were purchased from Sigma Aldrich. For immunohistochemistry (IMC), Trizma base solution (TBS), Trizma non saline (TNS) , 0.2% Triton X-100 in Trizma base solution (TXTBS), Phosphate buffer saline (PBS) 1X, 4% paraformaldehyde, MetOH , 3% Normal Horse Serum (NHS, S-2000), primary antibody, secondary antibodies , distilled water and cryoprotective media were prepared and utilized [27]. VECTASTAIN Elite ABC Kit (PK-6100) and DAB substrate kit (SK-4100) were obtained from Vector Laboratories, Inc. Burlingame, CA. Euthatal, xylene and DPX Mounting media (1330-20-7) were received from Merck.

2.2 Preparation of CaO nanoparticles

A simple and cost effective synthetic route was adopted to synthesize inorganic metal oxide nanoparticle using chemical co-precipitation [28, 29]. In this process drop by drop addition of an aqueous sodium hydroxide (NaOH) in an aqueous calcium chloride (CaCl_2) resulted in the supersaturated aqueous solution of CaO nanoparticles under vigorous stirring at 80°C for 60 minutes. The obtained white colloidal solution of calcium hydroxide ($\text{Ca}(\text{OH})_2$) was washed in hydro-alcoholic suspension to remove sodium chloride and enhanced its stability due to a lower degree of agglomeration [30]. The resulting suspension was passed across 0.45 μm filter syringe and dried at 60°C for 24 hours. These nanoparticles were annealed at 450°C and stored in a

desiccator box before use. The loading of CaO nanoparticles was achieved using the binding of polyvinyl alcohol (PVA) over CaO surface under constant thermal stirring [31]. Finally, a colloidal suspension of PVA coated CaO NPs was used to examine toxicity and localization with different antibodies.

2.3. Characterization

The structural phases and crystallite size were identified by employing PANalytical XPert PRO XRD diffractometer, θ -2 θ , equipped with Cu K α ($\lambda = 1.5406 \text{ \AA}$) radiations at 40 KV and 40 mA. The thermal analysis of CaO was monitored by thermogravimetric / differential scanning calorimetric (TGA-DSC) on SDT Q600 (TA instrument). The presence of functional groups was confirmed by SHIMADZU IR Prestige 21 spectrometer operated between 300-600 cm^{-1} to screen at room temperature. The morphology and compositional analysis were observed by JEOL 648OLV scanning electron microscope. The UV-Vis spectra were recorded by GENESYS 10S Spectrophotometer. Magnetic imaging resonance (MRI) acquisition was imaged using 4.7 T Magnetron BioSpec 47/40 System (Bruker Biospin GmbH, Ettlingen, Germany).

2.4 Toxicity Examination

SHR (Spontaneous hypertensive rats), ~ 5 weeks of age, were obtained from the University animal facility and individually housed in cages. All studies were conducted in accordance with UK Animals Scientific Procedures Act 1986 and The University of Cambridge Ethical Review Panel. All animals were kept under the standard conditions of temperature and provided with drinking water and commercial feed, ad libitum. SC injection (150 μl of coated CaO NPs in PBS buffer) was given to each rat [31] and regularly observed for any clinical signs of toxicity at weekly intervals. After three months, the experiment was terminated by sacrificing the rats using intra-peritoneal injection (30mg/100g) of sodium pentobarbitone. After reperfusion, brains were removed quickly and stored with 4% of paraformaldehyde for overnight (4°C). After that, brain tissues were kept in 30% sucrose for cryoprotection [27].

2.4.1. Histopathology

Tissue samples from the skin, muscle, liver, kidney and brain were fixed in 10% neutral phosphate buffered formalin. The preserved samples were processed with a series of ethanol dilutions. The histopathological examination was carried out using conventional hematoxylin and eosin (H&E) staining protocol on harvested tissues.

2.5. Localization of nanoparticles

Five male SHRs of age ~5 weeks were selected. The methodology was designed to utilize the minimum number of animals which were enough to obtain meaningful results. Middle-cerebral artery (MCA) of all rats was occluded for 15 min and then MRI scanning was done after 3 months of reperfusion of MCA. As MRI was completed, the experiment was discontinued by perfusion and fixation of brain for immunofluorescence assay.

2.5.1 Anesthesia

The rats were given general anesthesia with 4% isoflurane with combination of 0.3 l/min oxygen and 0.7 l/min nitrous oxide. This flow rate was kept constant with 2% isoflurane throughout the surgery. Rectal probe was used to monitor their body temperature and heating pad retained it at 37°C during the procedures. The continuous pulse rate and blood oxygen saturation were also monitored with a pulse oximeter.

2.5.2 Middle cerebral artery occlusion (MCAo)

The distal clip MCAo model was conducted by the method described by Buchan et al [32] as routinely used in our laboratory [33, 34]. The left common carotid artery (CCA) was explored through a midline incision over the neck and was ligated loosely with silk 4-0. An incision was given over a line extending between the outer corner of the right eye and an external auditory meatus. The temporalis muscle was excised to reach the base of skull. The left MCA was exposed

by making a 2-mm hole in front of the fusion of squamosal part of the skull and zygomatic arch. MCA was visualized by retracting dura mater where it passes over the inferior cerebral vein at the rhinal fissure. The MCA was clipped by a micro-aneurysmal clip no. 1, and after that the left CCA was ligated temporarily. This blockage over the MCA was removed after 15min and the wound closed after observing the blood flow through the artery [34]. All the animals were kept for three months and then euthanized.

2.5.3 Post procedure MRI

MRI was conducted after three months of toxicity testing before euthanizing the animals. Anesthesia comprising of 4% isoflurane in 0.3 l/min oxygen and 0.7 l/min nitrous was delivered to each animal for the acquisition of MRI and maintained with 1.5–2% isoflurane for the whole experiment while the body temperature of each rat was kept 37° C (Williamson et al., 2013). The same protocol was followed for MRI acquisition [27]. The post-exposure images were obtained after 3 months with a 4.7 T Magnetron. T2-weighted images were taken at TR = 3500 ms , TE = 36 ms , ELT 8 , slice thickness = 1mm, plane resolution = 0.156mm. Diffusion weighted images (DWI) were acquired with an EPI sequence at TR = 3000 ms , TE = 35 ms, 35 directions b = 1000s/mm², slice thickness = 1.5mm, plane resolution = 0.312mm.

2.5.4 Cryosectioning

After MRI, the brains were removed from the skull and overnight stored in 4% PFA solution (4°C), and immersed in 0.1 M PBS with 30% sucrose for 3-4 days. The whole brain harvested from each rat was placed onto a specimen shuttle of sledge microtome and sliced for coronal sections series (40µm). Different sections were taken from the forceps minor/ anterior forceps of corpus callosum to the superior colliculi (Bregma 3.7 to – 6.80 mm)) and the visual cortex and fixed on gelatin-coated slides [27].

2.5.5 Immunofluorescence for localization of nanoparticles

For immunofluorescence assay, brain cryosections were quenched with CH₃OH and H₂O₂ (10% , 5min) and kept in a solution containing 3% NHS in TXTBS (2 hours). 2ml solution of nanoparticles was prepared in PBS for specific bindings with different primary antibodies. Sections were overnight incubated at 4°C in this solution for the nuclear protein for mature neurons (NeuN, 1: 1000 ; MAB377 , Chemicon International) , macrophages and reactive microglia (OX42, 1:400; MCA275R, Serotec Ltd.) and astrocytes (GFAP, 1:500; G3893, Sigma-Aldrich company Ltd.). After then, sections were washed with TBS and incubated in TXTBS containing secondary antibody goat anti-mouse Cy3 (1: 150, Jackson ImmunoResearch, 2 hours). After washing, the sections were mounted on gelatin-coated slides, dried for 15 minutes on a heating block (40°C) and cover slipped using FluorSave reagent (Calbiochem).

2.5.6 Immunohistochemistry

The staining protocol for immunohistochemistry is same as used in immunofluorescence with the difference in the bindings with nanoparticles and secondary antibody. Briefly, the frozen sections were treated with CH₃OH and H₂O₂ (10 % , 5min) and 3% NHS in TXTBS (2 hours). Consecutive sections were incubated at 4°C with primary antibody in particular for the nuclear protein for mature neurons (NeuN, 1: 1000 ; MAB377 , Chemicon International) , macrophages and reactive microglia (OX42, 1:400; MCA275R, Serotec Ltd.) and astrocytes (GFAP, 1:500; G3893, Sigma-Aldrich company Ltd.). After washing with TBS (3x) , the sections were processed with biotinylated anti-mouse IgG (1:200 ; Vector, 2 hours) as secondary antibody and streptavidin horseradish peroxidase complex (ABC Kit, 10 min) and the final chromogen was visualized with Di-aminobenzidine (DAB Kit, 5 min). Finally, the sections were dehydrated through different grades of alcohol, cleared with xylene and the slides were cover-slipped with DPX mountant.

2.7 Microscopic assessment of ischemic lesions

The stained slides were scanned at 200x on Ariol SL-50 (Applied Imaging, Santa Clara, USA) and captured with a microscope (BX61, Olympus) integrated to the system. The composite images were automatically stitched from the individual frames.

3. Results and Discussion

Identification and purification of phases for as-prepared sample was analyzed by comparing XRD pattern of CaO with the standard database from International Centre for Diffraction Data.

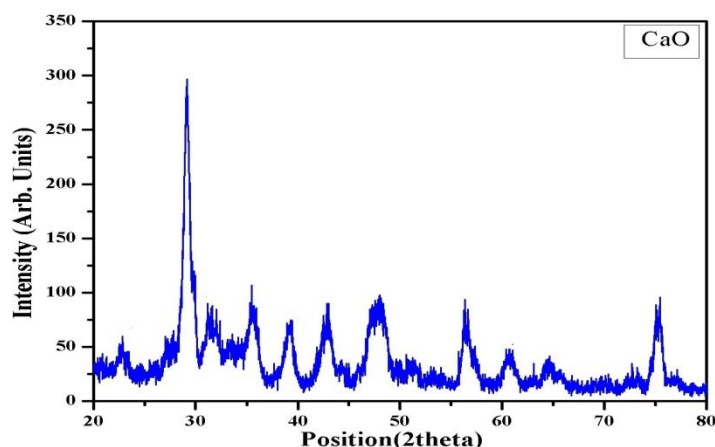


Fig. 1: X-ray diffraction pattern of CaO nanoparticles.

All the preferred orientations confirm the purity of CaO obtained in the present research. Fig. 1 confirms pure cubic phase of CaO and can be indexed through all the peaks with a Fm-3m space group (ICDD Card Nos. 00-004-0777&00-017-0912). The mean crystallite size was calculated using Debye Scherrer's formula [35]

$$\text{crystallite size} = \frac{0.94\lambda}{\text{FWHM} \cos\theta}$$

Where $\lambda = 1.54 \text{ \AA}$, is the wavelength of X-ray, FWHM is the broadening of the diffracted peak at half maxima and θ is the corresponding Bragg angle, and found to be $110 \text{ \AA} / 11 \text{ nm}$.

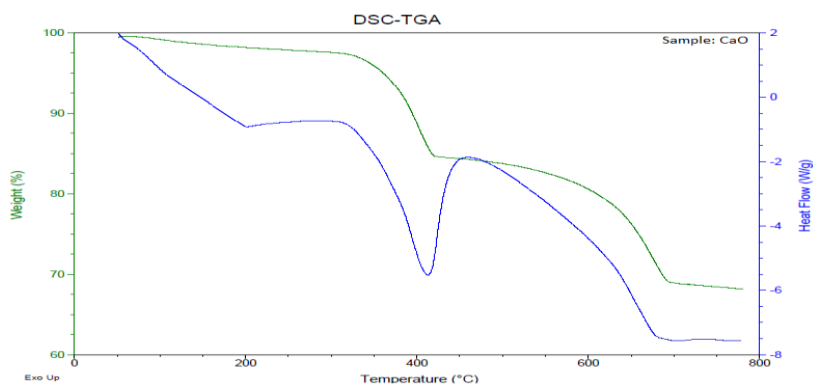


Fig. 2: Thermal Analysis of CaO nanoparticles.

Fig. 2 shows the thermal transitions during the reaction process were described by TGA/DSC. The figure indicates that the degradation in nanoparticles occurred in three phases, when the temperature is varied from 0°C to 800°C. Initially, mass loss occurs below 200°C due to the hydration of water contents. The second mass loss was found at 420°C attributing to the exhaustion of ethanol used in chemical reactions. The rapid mass change was observed in the third phase at 680°C. This change leads to the complete decomposition of $\text{Ca}(\text{OH})_2$ in CaO.

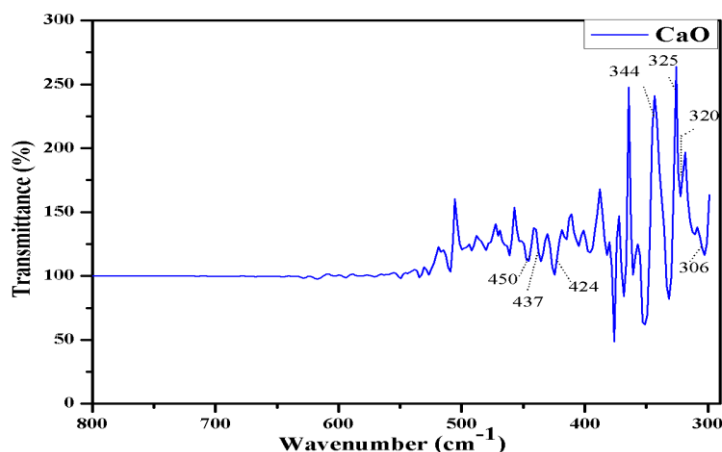


Fig. 3: FTIR spectra of CaO nanoparticles.

Fig. 3 demonstrates the characteristic absorption bands of CaO recorded within the range 300-800 cm^{-1} . In frequency distribution, the peaks at 306, 320, 325 and 344 cm^{-1} corresponds to the average value of lattice vibration [36]. The IR band peaked at 424 cm^{-1} may be due to vibrations in the CaO lattice as reported [37, 38]. The band appears 437 cm^{-1} is corresponded to C-H stretching [39]. The absorbed band at 450 cm^{-1} is also related to Ca-O bond [40]. Hence, the aforementioned bands affirm the presence of CaO with no other trace elements.

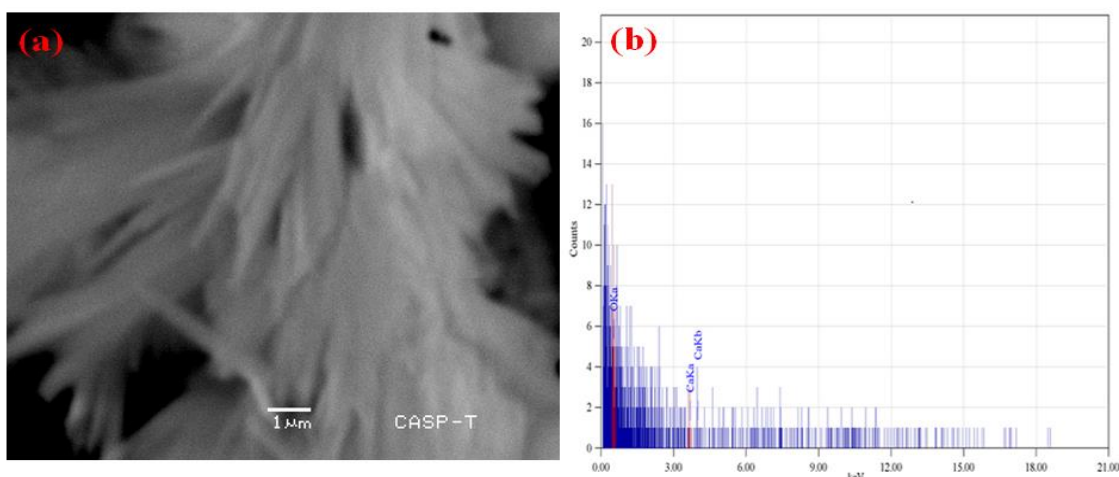


Fig. 4: SEM images (a) and EDX profile (b) of CaO.

The nanowires structure of CaO is illustrated in Fig. 4a whereas EDX provides an evidence of the only existence of Ca and O (Fig. 4b) given by EDX.

The optical absorption spectrum of CaO nanoparticles is shown in Fig. 5a. It can be seen from the figure that the absorption of CaO nanoparticles lies in the UV-region and no absorption in visible region. The linear band gap plotting of CaO nanoparticles was calculated around 4.17 eV as shown in Fig.5b which was confirmed by the absorption spectra. The reason for this increase/change is related to the smaller size of CaO nanoparticles as the optical properties are strongly dependent on the particle size [18]. The optical band gap was analyzed by plotting a graph between $(\alpha h\nu)^2$ as a function of $h\nu$

$$(\alpha h\nu)^2 = B(h\nu - E_g)^n$$

Where 'B' is constant, 'E_g' is an optical band gap of CaO and exponent 'n' is the nature of the transition. The estimated values of $n = 1/2, 2, 3/2, 3$ are assigned to direct, an indirect, forbidden direct and forbidden indirect transitions, respectively [41, 42].

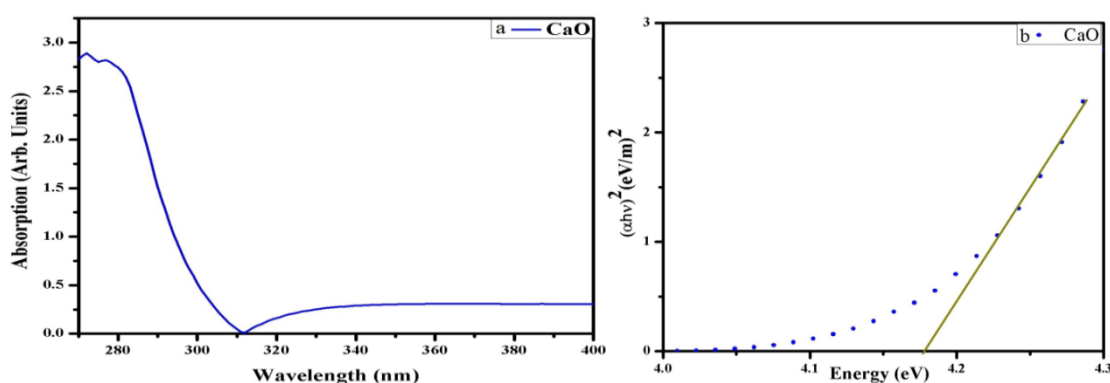


Fig. 5 (a): UV-Vis spectra of CaO nanoparticles (b) Plot of $(\alpha h\nu)^2$ versus Energy of CaO.

Histopathological evaluation

The inflammatory responses from the different organs on exposure to CaO nanoparticles were shown in Table 1. Skin tissues revealed no discernible lesions or degenerative changes and all three dermal layers, i.e., epidermis, dermis and hypodermis were fairly intact. Moreover, normal appearance of capillary structure and deformation in the pattern of collagen and elastic fibers was also observed. Likewise, no observable pathological changes were observed in the muscle samples from the majority of the animals and muscle fibers remained intact.

Table 1: Inflammatory grading among CaO exposed organs.

Nanoparticle	Skin	Muscle	Liver	Kidney	Brain
CaO	-	-	+	++	+

- : no remarkable change, + :mild change, ++ : excessive change

Histopathological photomicrographs of liver, kidney and brain are shown in Fig. 6 respectively, in order to investigate the potency of CaO nanoparticles to the tissue damage. In Fig. 6a, CaO augmented a number of morphologically distorted and disoriented hepatocytes was significantly evident all over the hepatic parenchyma, while the higher resolution investigation revealed severely distorted hepatocytes undergoing necrotic changes, which depicted pathological condition of sub-acute severe hepatic degeneration and necrosis.

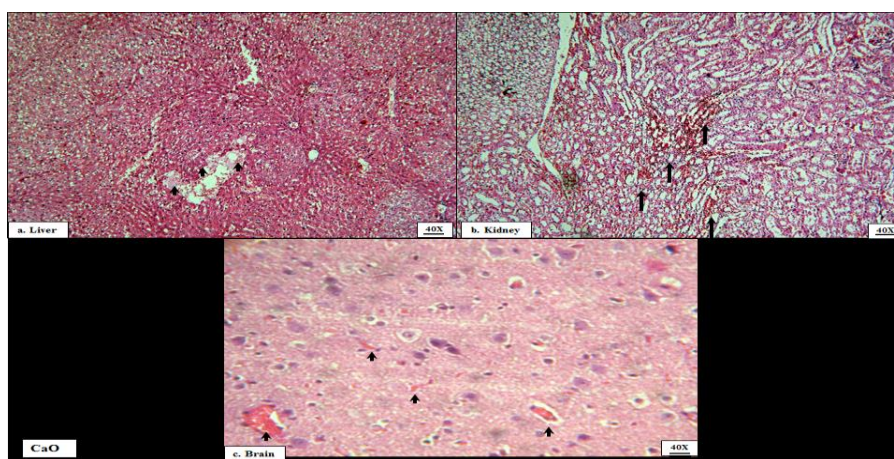


Fig. 6: Histopathological images harvested from liver, kidney and brain of rats 3 months post-exposure to CaO particles.

Fig. 6b shows that kidneys were affected by severe tubular hemorrhages represented with arrows, renal tubular necrosis and tubular parenchymatous degeneration. Moreover, histological investigations revealed that the renal tubular cells were distended, pyknotic, and were morphologically diagnosed as sub-acute severe renal tubular degeneration and necrosis. Similarly, few incidences of perivascular coughing and mild hemorrhages (arrows) were observed in brain sections of rat (Fig. 6c).

Localization of nanoparticles:

MRI acquisition:

DW1 and T2W MRI images (Fig. 7) showed no obvious pathology in the brain slices after 15 min of temporary MCAo, which is in confirmation that 15 min of occlusion only produce subtle neuro-inflammation which cannot be detected in current MRI modalities.

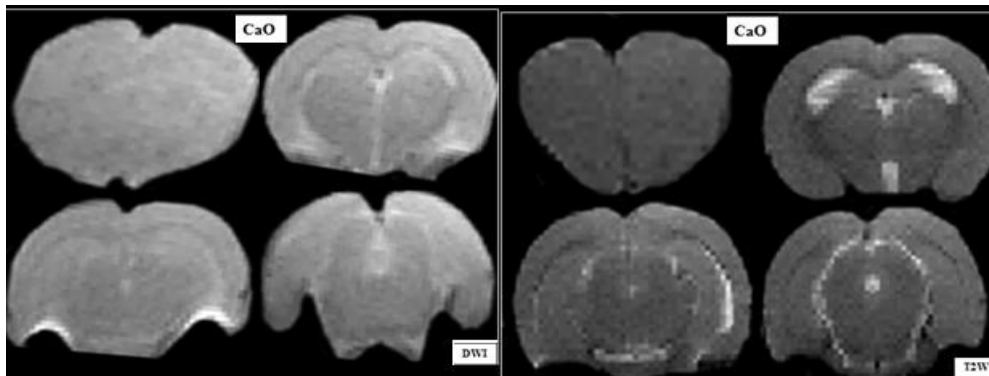


Fig. 7: Coronal MR Images of a rat brain after reperfusion with CaO NPs.

Immunofluorescence and Immunohistochemistry

Since no lesions and inflammations were detected, hence, immunofluorescence and immunohistochemistry assay were performed to determine whether or not prepared nanoparticles conjugated with different anti-bodies could localize this stable neuro-inflammation. In Fig. 8, no binding was detected in the NeuN, OX42 and GFAP antibodies labelled with CaO nanoparticles. This absence of binding is attributed to the antimicrobial activity of CaO as in literature [18, 22 and 23].

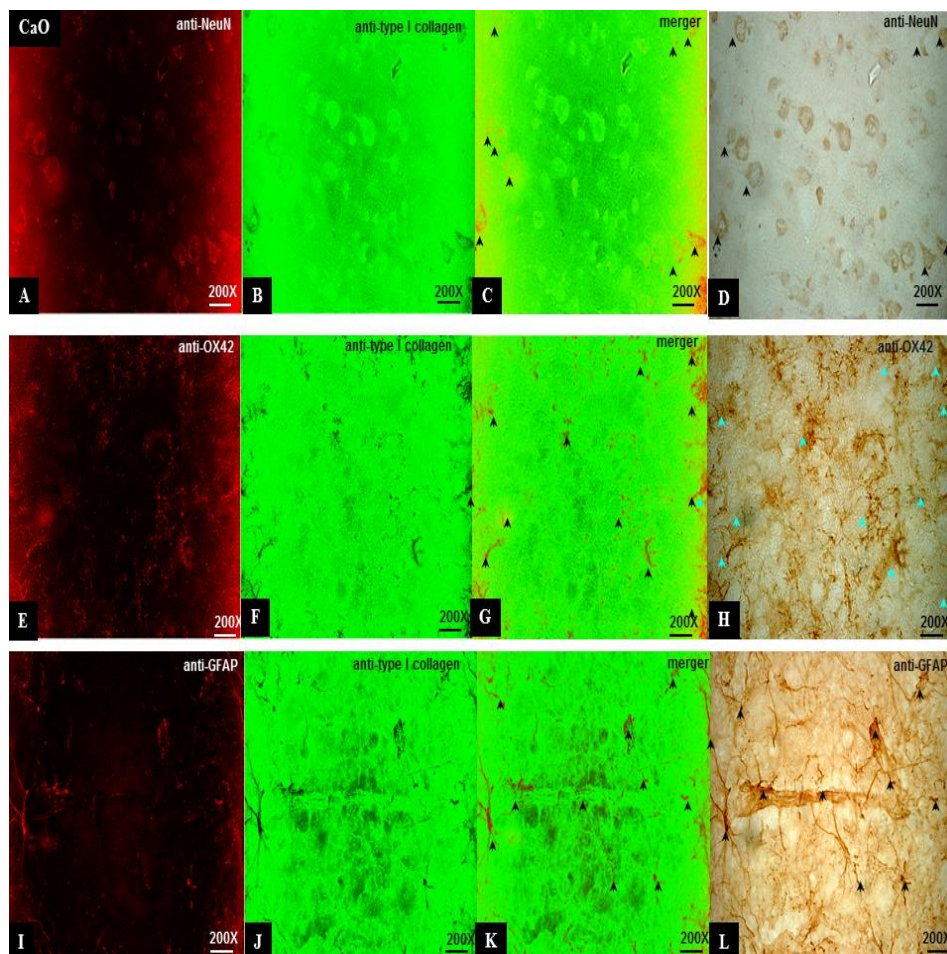


Fig. 8: Conjugation potential of CaO nanoparticles with neuronal, microglial and astrocytic receptors in rat brain. Anti-type I collagen is used just to determine cellular architecture to get immunofluorescence images.

4. Conclusion

In this work, CaO nanoparticles were prepared by chemical co-precipitation and made functionalized in polyvinyl alcohol solution. The XRD pattern revealed that the particle size of CaO was ~ 11 nm. The absorption spectrum of nanoparticles shows the absorption in UV-region due to a large band gap of CaO. The acute toxicity of CaO NPs in rats was investigated using H&E staining protocols. Sub-acute severe hepatic and tubular degenerations were observed in liver and kidney respectively. MRI shows no obvious lesions in the brain of rats. The mild hemorrhages can be seen in the brain, which is attributed to the fact of crossing blood brain barrier. It was found that CaO bonding with antibodies not detected in immunofluorescence image and showing antimicrobial nature. It is suggested that CaO NP's cannot be used directly with antibodies; they need to be modified with appropriate hydrophilic coating. However, these assessments require further and careful studies.

Acknowledgment

The author would like to acknowledge Higher Education Commission, Pakistan for financial support through IRSIP at Cambridge University UK and "Indigenous Ph.D Fellowship Program (5000 Fellowships)". Special thanks to Dr. Iftikhar Ahmad Butt (Medical Officer & Registrar, Mayo Hospital Lahore, Pakistan) and Dr. Munir Ahmad (Nuclear Specialist, Institute of Nuclear Medicine and Oncology Lahore INMOL, Lahore, Pakistan) and Khalid Rashid (Scientific Officer, Pakistan Council of Scientific and Industrial Research (PCSIR), Lahore, Pakistan) for kind guidance in this manuscript.

References

- [1] P. Li, C. Nan, Z. Wei, J. Lu, Q. Peng, Y. Li, *Chemistry of Materials*, **22**, 4232(2010).
- [2] F. Tian, A. P. Mello, G. Estrada, et al., *Nanotoxicology*, **2**, 232(2008).
- [3] R. L. Edelstein, C. R. Tamanaha, P. E. Sheehan, et al., *Biosensors and Bioelectronics*, **14**, 805(2000).
- [4] J. M. Nam, C. S. Thaxton, C. A. Mirkin, *Science*, **301**, 1884(2003).
- [5] D. Cui, F. Tian, Y. Kong, C. Ozkan, I. Titushikin, H. Gao, *Nanotechnology*, **15**, 154 (2004).
- [6] R. S. Molday, D. Mackenzie, *Journal of Immunological Methods*, **52**, 353(1982).
- [7] R. Weissleder, G. Elizondo, J. Wittenberg, C. A. Rabito, H. H. Bengel, L. Josephson, *Radiology*, **175**, 489(1990).
- [8] A. C. Eifler, C. S. Thaxton, *Biomedical Nanotechnology: Methods and Protocols, Methods in Molecular Biology*, **726**, 325(2011).
- [9] Z. Cheng, A. Al-Zaki, J. Z. Hui, V. R. Muzykantov, A. Tsourkas, *Science*, **338**, 903(2012).
- [10] V. Biju, *Chemical Society Review*, **43**, 744(2014).
- [11] E. Neuwelt, N. J. Abbott, L. Abrey, et al., *The Lancet Neurology*, **7**, 84(2008).
- [12] W. M. Pardridge, Why is the global CNS pharmaceutical market so underpenetrated?. *Drug Discovery Today*, **7**, 5(2002).
- [13] M. W. Bradbury, D. J. Begley, J. Kreuter, *The Blood-Brain Barrier and Drug Delivery to the CNS*. 1st Edition. Informa Healthcare (Marcel Dekker), Inc. USA. (2000).
- [14] S. Bhaskar, F. Tian, T. Stoeger, et al., *Particle and Fibre Toxicology*, **7**, 25 pages(2010).
- [15] H. C. Huang, S. Barua, G. Sharma, S. K. Dey, K. Rege, *Journal of Controlled Release*, **155**, 344(2011).
- [16] J. Safari, Z. Zarnegar, *Journal of Saudi Chemical Society*, **18**, 85(2014).
- [17] W. Feng, L. D. Sun, Y. W. Zhang, C. H. Yan, *Coordination Chemistry Reviews*, **254**, 1038(2010).
- [18] P. N. Nirmala, G. Suresh, *International Journal of Recent Scientific Research*,

- 4**, 1320(2013).
- [19] L. Qi, Coordination Chemistry Reviews, **254**, 1054(2010).
- [20] D. B. Kuang, A. W. Xu, Y. P. Fang, H. Q. Liu, C. Frommen, D. Fenske, Advanced Materials, **15**, 1747(2003).
- [21] F. Kim, S. Connor, H. Song, T. Kuykendall, P. Yang, Angewandte Chemie International Edition, **43**, 3673(2004).
- [22] M. R. Leonardo, M. E. Hernandez, L. A. Silva, M. T. Filho, Oral Radiology and Endodontology, **102**, 680(2006).
- [23] Z. Mohammadi, P. M. Dummer, International Endodontic Journal, **44**, 697(2011).
- [24] G. Hasselgren, B. Olsson, M. Cvek, Journal of Endodontics, **14**, 125(1988).
- [25] K. E. Safavi, F. C. Nichols, Journal of Endodontics, **19**, 76(1993).
- [26] J. M. Tanomaru, M. R. Leonardo, T. M. Filho, I. B. Filho, L. A. Silva, International Endodontic Journal, **36**, 733(2003).
- [27] S. Ejaz, D. J. Williamson, T. Ahmed, et al., Neurobiology of Disease, **51**, 120(2013).
- [28] V. Daniele, G. Taglieri, R. Quaresima, Journal of Cultural Heritage, **9**, 294(2008).
- [29] S. Datta, D. J. W. Grant, Crystal Research and Technology, **40**, 233(2005).
- [30] G. Taglieri, C. Mondelli, V. Daniele, E. Pusceddu, G. Scoccia, Advances in Materials Physics and Chemistry, **4**, 50(2014).
- [31] H. Yang, C. Zhang, X. Shi, et al., Biomaterials, **31**, 3667(2010).
- [32] A. M. Buchan, D. Xue, A. Slivka, Stroke, **23**, 273(1992).
- [33] M. Takasawa, J. S. Beech, T. D. Fryer, et al., Journal of Cerebral Blood Flow & Metabolism. 2007; **27**, 679(2007).
- [34] J. L. Hughes, J. S. Beech, P. S. Jones, D. Wang, D. K. Menon, J. C. Baron, NeuroImage, **49**, 19(2010).
- [35] B. D. Cullity, S. R. Stock, Elements of X-ray Diffraction. 3rd Edition. Prentice Hall. New Jersey, (2001).
- [36] J. T. Gourley, W. A. Runciman, Journal of Physics C: Solid State Physics, **6**, 583 (1973).
- [37] A. Imtiaz, M. A. Farrukh, M. Khaleeq-ur-rahman, R. Adnan, The Scientific World Journal, Hindawi Publishing Corporation, **2013**, 11 pages (2013).
- [38] M. I. Zaki, H. Knozinger, B. Tesche, G. A. H. Mekhemer, Journal of Colloid and Interface Science, **303**, 9 (2006).
- [39] Maruthamuthu, S. P. Prabhavathi, Ranjith, S. Rajam, K. Raja, World Journal of Pharmaceutical Research, **3**, 362(2014).
- [40] M. Sadeghi, M. H. Hussein, Journal of Applied Chemical Research, **7**, 39 (2013).
- [41] A. Gaber, A. Y. Abdel Latief, M. A. Abdel-Rahim, M. N. Abdel-Salam, Materials Science in Semiconductor Processing, **16**, 1784 (2013).
- [42] E. Filippo, D. Manno, A. R. De Bartolomeo, A. Serra, Journal of Crystal Growth, **330**, 22 (2011).